

High-angle active conjugate faults in the Anza-Borrego shear zone, Southern California

Xiaoyu Zou¹, Yuri Fialko¹, Andrew Dennehy², Alexander Cloninger^{3,4},
Shabnam J. Semnani⁵

¹Institute of Geophysics and Planetary Physics, Scripps Institution of Oceanography, University of California San Diego, La Jolla, CA 92093, USA.

²Committee on Computational and Applied Mathematics, University of Chicago, Chicago, IL 60615, USA.

³Department of Mathematical Sciences, University of California San Diego, La Jolla, CA 92093, USA.

⁴Halicioğlu Data Science Institute, University of California San Diego, La Jolla, CA 92093, USA

⁵Department of Structural Engineering, University of California San Diego, La Jolla, CA 92093, USA.

Key Points:

- We use a new algorithm to identify quasi-linear clusters of micro-earthquakes associated with active strike-slip faults in a trans-tensional region south of the Salton Sea, Southern California.
- The observed dihedral angles between right- and left-lateral faults show a broad distribution with a peak around 70°.
- Non-optimal fault orientations can be explained by tectonic rotation due to a long-term slip on a more mature system of right-lateral faults.

Abstract

Orientations of active antithetic faults can provide useful constraints on in situ strength of the seismogenic crust. We use LINSKAN, a new unsupervised learning algorithm for identifying quasi-linear clusters of earthquakes, to map small-scale strike-slip faults in the Anza-Borrego shear zone, Southern California. We identify 332 right- and left-lateral faults having lengths between 0.1-3 km. The dihedral angles between all possible pairs of conjugate faults are nearly normally distributed around 70 degrees, with a standard deviation of ~ 30 degrees. The observed dihedral angles are larger than those expected assuming optimal fault orientations and the coefficient of friction of 0.6-0.8, but similar to the distribution previously reported for the Ridgecrest area in the Eastern California Shear Zone. We show that the observed fault orientations can be explained by fault rotation away from the principal shortening axis due to a cumulated tectonic strain.

Plain Language Summary

Small earthquakes can highlight the location and attitude of active faults at depth. We use a large set of earthquake locations and a novel algorithm to identify small faults, along with their orientations, and sense of slip. We find that faults with opposite sense of slip (the so-called antithetic, or conjugate faults) are at nearly right angles to each other. For newly created faults, such a configuration would imply that friction is almost negligible. We suggest that the high-angle conjugate faults instead result from fault rotation due to long-term tectonic deformation.

Introduction

According to the Mohr-Coulomb failure theory, new or pre-existing faults should be preferentially activated at an angle $\pm\theta_0$ to the principal compression axis (Anderson, 1951; Sibson, 1974; Scholz, 2019). The two antithetic fault orientations are known as conjugate faults (e.g., Twiss & Moores, 1992, p. 141). For typical laboratory values of the static coefficient of friction μ of 0.6-0.8 (Byerlee, 1978), the dihedral angle between optimally oriented conjugate faults is $2\theta_0 = \arctan(\mu^{-1}) \approx 50 - 60$ degrees (Anderson, 1951; Sibson, 1974). While in some cases there is good agreement between predictions of the Mohr-Coulomb theory and the observed fault orientations (Walsh & Watterson, 1988; Alt & Zoback, 2017), there are also ample examples of conjugate faults that are not optimally oriented with respect to each other and/or the inferred principal stress axes,

51 assuming the Byerlee's friction. In fact, many active conjugate faults exhibit dihedral
 52 angles close to 90 degrees, considerably greater than $2\theta_0$ (McGill et al., 1989; Thatcher
 53 & Hill, 1991; Yue et al., 2012; Jin & Fialko, 2020; Fialko & Jin, 2021; Hatch-Ibarra et
 54 al., 2022). Proposed explanations include anomalously low in situ friction (e.g., Middle-
 55 ton & Copley, 2014; Ross et al., 2019), a dominant control of deep fault roots in the duc-
 56 tile lower crust (Thatcher & Hill, 1991; Scholz & Choi, 2022; Liang et al., 2021), and fault
 57 rotation due to finite tectonic strain (Cloos, 1955; Freund, 1970; Nur et al., 1986; Fialko
 58 & Jin, 2021). A low frictional strength is often inferred in case of mature well-slipped
 59 faults (Mount & Suppe, 1987; Wernicke, 1995; Sibson, 1994), presumably due to acti-
 60 vation of various weakening mechanisms (Rice, 2006; Di Toro et al., 2011; Brown & Fi-
 61 alko, 2012). However, the bulk of the seismogenic upper crust is unlikely extremely weak,
 62 as evidenced by optimal orientations of at least some active faults (Walsh & Watterson,
 63 1988; Alt & Zoback, 2017), stress measurements in deep boreholes (Townend & Zoback,
 64 2000), and long-term support of topography (Coblentz et al., 1994; Burov, 2011; Fialko
 65 et al., 2005). Deep ductile roots could possibly control the orientation of faults that orig-
 66 inate at the bottom of the seismogenic zone and/or cut through the entire brittle crust
 67 (Scholz & Choi, 2022), but not of the abundant small faults having characteristic dimen-
 68 sions of less than ~ 10 km that are unlikely connected to the ductile substrate (Fialko
 69 & Jin, 2021). It was also suggested that faults may typically form at near-optimal an-
 70 gles, but be subsequently rotated away from the axis of maximum compressive stress due
 71 to finite tectonic strain (Cloos, 1955; Freund, 1970; Fialko & Jin, 2021). The maximum
 72 rotation angle is limited by a fault lock-up, and is on the order of θ_0 (Nur et al., 1986;
 73 Sibson, 1990).

74 These hypotheses can be discriminated by quantifying relative orientations of small
 75 active faults. Fialko and Jin (2021) noted that lineated clusters of microseismicity in the
 76 Eastern California Shear Zone near Ridgecrest reveal multiple high-angle conjugate faults
 77 consistent with the rupture geometry of the M6.4 foreshock and M7.1 mainshock of the
 78 2019 Ridgecrest earthquake sequence (Ross et al., 2019; Jin & Fialko, 2020; Fialko, 2021).
 79 Fialko and Jin (2021) further showed that the observed fault geometries are consistent
 80 with finite strain and rotation since the inception of the Eastern California Shear Zone.
 81 It is of interest to quantify relative orientations of conjugate faults in different regions
 82 undergoing active deformation (Fialko, 2021). However, identifying and systematically

mapping active fault structures is a challenging task, especially in case of relatively small faults that typically do not have a surface expression.

In this paper, we apply a new algorithm to map out a population of active strike-slip faults in the Anza-Borrego shear zone in Southern California, and evaluate the distribution of dihedral angles between the identified sets of antithetic (i.e., left- and right-lateral) faults. We then use the observed fault orientations to evaluate possible controlling mechanisms.

1 Data and Methods

Active faults are often expressed in microseismicity (Valoroso et al., 2009; Nadeau & McEvilly, 1999). In case of strike-slip faults, the associated microearthquakes appear as localized streaks of epicenters in a map view (e.g., Alt & Zoback, 2017; Fialko, 2021). The respective quasi-linear clusters (QLCs) of events can be used to map active fault structures (Skoumal et al., 2019; Fialko, 2021). Several algorithms were proposed to identify lineated structures in highly scattered point clouds, all based on the point density and/or Euclidian distance between candidate points (Skoumal et al., 2019; Cochran et al., 2020; Fialko, 2021). In particular, Fialko (2021) used a non-parametric unsupervised learning algorithm OPTICS (Ordering Points To Identify the Clustering Structure; Ankerst et al., 1999), a variant of DBSCAN (Schubert et al., 2017), to separate clustered events from the background seismicity. One of the drawbacks of proximity-based algorithms such as OPTICS and DBSCAN is that the selected clusters can be of arbitrary shape, and additional screening is needed to cull out clusters having isometric or irregular geometries. Oftentimes such clusters contain smaller-scale lineated features that could be sensibly associated with active faults but would be missed by the search algorithm if the parental cluster is culled out. A robust procedure for multi-scale identification of quasi-linear sets of epicenters is therefore highly warranted.

1.1 LINSKAN Algorithm

We use LINSKAN, a new algorithm based on OPTICS, in which the Euclidean distance metric is replaced with a distance function $D(P, Q)$ derived from Kullback-Leibler (KL) divergence. The KL divergence is a measure of how similar two given distributions are. For two groups of points P and Q , the distance function $D(P, Q)$ is minimized when

points in both groups are distributed along similar directions (see Supplementary Information for details). This ensures that only specific geometric shapes (in this case, QLCs) are selected. We evaluated the accuracy and robustness of the algorithm using a synthetic catalog of earthquake epicenters. The synthetic catalog consists of (i) arbitrarily oriented QLCs of various sizes, (ii) quasi-isometric clusters, and (iii) randomly distributed “background seismicity” (see Figure S1a in the Supplementary Information). The LINS-SCAN algorithm is able to efficiently identify and separate QLCs from the rest of the data (Figure S1b). Occasionally, some of the original QLCs are split into co-linear sub-segments (Figure S1b). This is not a major issue since we are interested in accurate estimation of the fault strike angles. If needed, adjacent QLCs can be merged by considering their proximity and along-strike continuity. More importantly, the algorithm is able to identify overlapping and intersecting clusters that are ubiquitous in the case of complex fault systems (e.g., Fialko, 2021), although for some of the overlapping clusters the selection choices are non-unique. In the test shown in Figure S1, the number of points identified as belonging to QLCs (Figure S1b) is about 80% of the total number of “true” QLC points in the input data set (Figure S1a). A small fraction of points was identified as QLCs even though they did not belong to any of the input QLCs, due to either false detections or spontaneous quasi-linear patterns in the randomly generated “background seismicity”.

1.2 Data analysis

We apply LINS-SCAN to quantify relative orientations of small strike-slip faults in a region of active deformation to the south of the Salton Sea, Southern California (Figure 1). This region accommodates ~ 20 mm/yr of strike-slip motion between the North American and Pacific plates (Tymofeyeva & Fialko, 2018), and hosts a number of active faults of various degrees of maturity (Jennings & Bryant, 2010), as well as abundant microseismicity (Yang & Hauksson, 2013). This region, hereafter referred to as the Anza-Borrego shear zone, is part of a transtensional transition zone connecting the Southern San Andreas Fault system to the Cerro Prieto fault system, and ultimately to the Gulf of California (Herzig & Jacobs, 1994; Crowell et al., 2013; Gonzalez-Ortega et al., 2014). We use a recently published catalog of precisely located events with focal mechanisms that spans 1981-2021 (Cheng et al., 2023). The event locations are shown in Figure 1. We convert geographic coordinates to the local Cartesian (UTM) coordinates using a lo-

cal origin at 117°W, 32°N. The catalog epicenters and the QLCs selected by LINSKAN are shown in Figure S4 (blue and orange dots, respectively).

To ensure that the selected QLCs are robust, we perform several quality checks. As spurious linear patterns may emerge at the boundaries of the area of interest (due to the discarding of data outside of the bounding box), we removed all east-west and north-south striking clusters near the respective boundaries. For each “inside” cluster, we compute the Pearson correlation coefficient $r = \sum_i (x_i - \bar{x})(y_i - \bar{y}) / \sqrt{\sum_i (x_i - \bar{x})^2 \sum_i (y_i - \bar{y})^2}$, where x_i, y_i are coordinates (northings and eastings) of each epicenter, and \bar{x}, \bar{y} are the means of x, y coordinates of events comprising a given cluster (e.g., Artusi et al., 2002). We retain clusters for which the absolute value of the correlation coefficient is greater or equal to 0.5. We further fit a straight line segment to the respective sets of points for each cluster, and compute the mean normalized distance δ between the points and the best-fit line as the mean of distances from the points to the line, divided by the line length. We discard clusters for which $\delta > 0.1$. Since we are interested in strike-slip faults, we discard clusters for which the dip angle of either P or T axis is greater than 40°. Finally, we perform a visual check to discard clusters in which the events are too sparse, unevenly distributed, hard to distinguish from the background seismicity, or organized in sub-clusters with significantly different orientations. Figure S2 shows several examples of the culled out “low quality” clusters, and Figures 3 and S5-S16 show QLCs that satisfy the above criteria. Out of the 1181 QLCs initially identified by LINSKAN (Figure S4), 332 QLCs passed the quality checks, and were used in the subsequent analysis.

To separate the sets of right- and left-lateral faults, for each QLC we compute composite focal mechanisms by summing up the moment tensors of individual events normalized by their scalar moments (Fialko, 2021). Given the fault plane (revealed by the QLC strike) and polarity of the composite focal mechanism, we determine the sense of slip on each identified fault. Consistent with the approximately north-south orientation of the principal strain rate axis (Figure S3), right-lateral faults strike predominantly north-west, and left-lateral faults strike predominantly north-east (Figure 4). Figure 2 shows the locations of the identified right- and left-lateral faults (red and blue dots, respectively). In total, there are 195 left-lateral faults and 137 right-lateral faults. The left-lateral faults have predominant strikes of $\sim 20\text{--}30^\circ$, and right-lateral faults strike between $\sim 300\text{--}340^\circ$ (Figure 4). The dominant orientations of active faults shown in Figure 4 are consistent with orientations of the right- and left-lateral Quaternary fault traces in our study area

(Figure 1). The dihedral angles between the identified QLCs (Figure 2) are calculated by taking the difference in fault strikes for every possible pair of right- and left-lateral faults (Fialko, 2021). Figure 5 shows the resulting distribution of dihedral angles. Similar results are obtained when we limit the distance between conjugate faults to be less than 5 km, although the number of samples is substantially reduced.

2 Discussion

The calculated dihedral angles are nearly normally distributed with a peak around 70° (Figure 5). The majority of the identified conjugate faults are thus at higher angles compared to optimal orientations predicted based on the Mohr-Coulomb theory (Anderson, 1951; Sibson, 1974), and observed e.g. in areas of fluid-induced seismicity in the central US (e.g., Alt & Zoback, 2017; Schoenball & Ellsworth, 2017; Skoumal et al., 2019), but similar to those observed in the Ridgecrest area of the Eastern California Shear Zone (e.g., Ross et al., 2019; Fialko & Jin, 2021; Fialko, 2021). The characteristic dimensions of faults or active fault patches used in our analysis vary from 75 m to 3 km, with the mean value of 0.5 km (Figures S4–S16). Rupture dimensions of individual earthquakes comprising the respective earthquake clusters are smaller still. The small rupture size has several implications. First, a substantial fraction of the identified small-scale ruptures are not associated with mature well-slipped faults, and thus not linked to the ductile substrate, precluding a possibility that their orientations are controlled by localized shear zones below the brittle-ductile transition (e.g., Takeuchi & Fialko, 2012, 2013; Fialko & Jin, 2021; Scholz & Choi, 2022; Liang et al., 2021). Second, small ruptures are not expected to produce strong dynamic weakening, so that their strength may be to the first order governed by quasi-static friction (e.g., Lapusta & Rice, 2003; Fialko, 2015).

In the area of interest, the principal axes of both the maximum horizontal shortening rate (Figure S3) and maximum compressive stress (Yang & Hauksson, 2013) are oriented approximately north-south. Results shown in Figure 4 indicate that populations of right- and left-lateral faults are not symmetrically distributed around the axis of the maximum shortening rate and/or compression. While most of the right-lateral faults are at angles of 45 ± 15 degrees to the principal strain rate/stress axis (Figure 4), most of the left-lateral faults are at more acute angles of $20\text{--}30^\circ$, nearly optimally oriented assuming the Byerlee’s law (i.e., the coefficient of friction of 0.6–0.8). This is different from the observed fault orientations in Ridgecrest, where the dihedral angles between conjugate

faults are approximately bisected by the principal strain rate and stress axes (Fialko & Jin, 2021; Fialko, 2021).

Assuming that the currently active left- and right-lateral faults initially formed at equal angles to the principal compression axis, and that their relative orientations with respect to each other have not changed over time, the data shown in Figure 4 might be interpreted as indicating a counter-clockwise rotation of the entire fault system by 10-15 degrees. One possible mechanism for such rotation is a preferred development and growth of right-lateral faults. It is known that slip on a fault embedded in an elastic medium results in fault rotation,

$$\omega = \arctan \left(\frac{1 - 2\nu}{2G} \Delta\tau \right), \quad (1)$$

where ω is the rotation angle in radians, G the shear modulus, ν the Poisson's ratio, and $\Delta\tau$ the stress drop (Martel, 1999). For an infinitely long strike-slip fault with a constant stress drop, the relation between the stress drop $\Delta\tau$ and surface fault slip s is:

$$\Delta\tau = \frac{1}{2} \frac{sG}{D}, \quad (2)$$

where D is the fault locking depth (e.g., Segall, 2010, p. 96). From equations 1 and 2, a strike-slip fault with a total offset s rotates by an angle

$$\omega = \arctan \left(\frac{1 - 2\nu}{4} \frac{s}{D} \right). \quad (3)$$

For right-lateral slip, the predicted sense of rotation is counter-clockwise (Martel, 1999). The estimated total offset on the San Jacinto Fault system that dominates interseismic deformation in the study area is 20-25 km (e.g., Morton & Matti, 1993). For $\nu = 0.25$ and $D = 12$ km (Lindsey et al., 2014; Tymofeyeva & Fialko, 2018), equation 3 suggests a rotation of 12-15 degrees. Using a depth-averaged slip instead of surface slip in equation 3 reduces the estimated rotation by a few degrees. This is a lower bound on the total possible rotation amount because it neglects contributions from other major faults such as the Elsinore fault, as well as the distributed deformation due to numerous small faults in the bulk of the brittle upper crust (e.g., Fialko & Jin, 2021).

A common rotation away from the optimal orientation however suggests θ_0 of 35 degrees, and $\mu < 0.4$, lower than predicted by the Byerlee's law. Another possibility is that the relatively small and immature left-lateral faults are optimally oriented assuming Byerlee's friction. The same may be true for immature right-lateral faults, however

the QLCs that are associated with major right-lateral faults (Figure 2) likely owe their orientations to the long-term fault rotation, as discussed above.

We interpret differences between the observed distributions of dihedral angles in different tectonic areas in terms of the amount of a total accommodated strain. In case of injection-induced seismicity in the central US (Alt & Zoback, 2017; Schoenball & Ellsworth, 2017; Skoumal et al., 2019), pre-existing faults are brought to failure due to increases in the pore fluid pressure, resulting in a preferential activation of faults that are optimally oriented with respect to the background stress. The Ridgecrest, eastern California, region is a developing shear zone, where new and pre-existing faults are continually activated and rotated primarily via distributed failure and simple shear (Fialko & Jin, 2021). The Anza-Borrego shear zone exemplifies a “high strain” end-member, whereby much of the deformation and rotation (Hauksson et al., 2022) is accommodated by well-developed plate boundary faults. The main difference between the observed orientations of small active faults in the Ridgecrest area of the Eastern California Shear Zone and the Anza-Borrego Shear Zone is that the latter features a non-symmetric distribution of conjugate faults with respect to the principal compression and shortening rate axes (Figure 4), likely due to different amounts of slip accommodated by the respective fault systems. At the initial stages of the shear zone development, synthetic (right-lateral) faults are rotated less than the antithetic (left-lateral) faults (Fialko & Jin, 2021) and are thus favored to grow. A continued slip on mature right-lateral faults rotates immature left-lateral faults toward the principal compression axis, which may eventually deactivate the rotated left-lateral faults and initiate slip on new or pre-existing left-lateral faults that are more optimally oriented for failure. Mature well-slipped faults may also develop deep crustal “roots” (Takeuchi & Fialko, 2012; Leloup et al., 1995; Jin et al., 2023) which can stabilize the fault orientation at ~ 45 degrees to the principal shortening axis (i.e., optimal for ductile shear), potentially explaining the observed near-orthogonal orientations of mature conjugate faults (Thatcher & Hill, 1991; Yue et al., 2012; Fialko & Jin, 2021). Under this model, deep shear zones are the consequence, rather than the cause, of fault development in the brittle upper crust.

3 Conclusions

We used a new algorithm to quantify orientations of small active faults at the southern end of the San Andreas-San Jacinto fault system, referred to as the Anza-Borrego

shear zone. The dihedral angles between conjugate strike-slip faults are nearly normally distributed with a mean value of $\sim 70^\circ$. The fault strikes are asymmetrically distributed with respect to the principal strain rate and stress axes, with left-lateral faults optimally oriented for failure assuming the Byerlee's law, and right-lateral faults rotated by ~ 10 - 20° counter-clockwise from the optimal orientation. We argue that the observed high-angle conjugate faults are not due to either low coefficient of friction or ductile shear zones in the lower crust, but can instead be explained by rotation due to a long-term tectonic deformation. Faults may form or be activated at near-optimal orientations, and subsequently rotate away from the principle shortening axis. A comparison to other areas of well-documented small active faults reveals an increase in the average dihedral angle with the total accumulated tectonic strain. We attribute the observed asymmetric distribution of conjugate faults with respect to the principal strain rate axis to a difference in the total amount of slip accommodated by the right- and left-lateral fault systems.

Acknowledgments

We thank the two anonymous reviewers for thoughtful comments that helped improve this manuscript. This study was supported by grants from NSF (EAR-1841273) and NASA (80NSSC22K0506) to YF. Figures were produced using Generic Mapping Tools (GMT) (Wessel et al., 2013) and Matlab. The authors declare no competing interests.

Data Availability Statement

LINSCAN source codes with examples and the QLC data used in our analysis are available at <https://doi.org/10.5281/zenodo.8356590>

References

- Alt, R., & Zoback, M. (2017). In situ stress and active faulting in Oklahoma. *Bull. Seism. Soc. Am.*, *107*, 216–228.
- Anderson, E. M. (1951). *The dynamics of faulting and dike formation with application to Britain*. Edinburgh: 206 pp., Oliver and Boyd.
- Ankerst, M., Breunig, M. M., Kriegel, H.-P., & Sander, J. (1999). Optics: ordering points to identify the clustering structure. *SIGMOD record*, *28*(2), 49–60.
- Artusi, R., Verderio, P., & Marubini, E. (2002). Bravais-Pearson and Spearman correlation coefficients: meaning, test of hypothesis and confidence interval. *The*

- 299 *International journal of biological markers*, 17, 148–151.
- 300 Brown, K. M., & Fialko, Y. (2012). "Melt welt" mechanism of extreme weakening of
301 gabbro at seismic slip rates. *Nature*, 488, 638–641.
- 302 Burov, E. B. (2011). Rheology and strength of the lithosphere. *Marine and*
303 *Petroleum Geology*, 28, 1402–1443.
- 304 Byerlee, J. (1978). Friction of rock. *Pure Appl. Geophys.*, 116, 615–626.
- 305 Cheng, Y., Hauksson, E., & Ben-Zion, Y. (2023). Refined earthquake focal mecha-
306 nism catalog for Southern California derived with deep learning algorithms. *J.*
307 *Geophys. Res.*, 128, e2022JB025975.
- 308 Cloos, E. (1955). Experimental analysis of fracture patterns. *Bull. Seism. Soc. Am.*,
309 66, 241–256.
- 310 Coblenz, D. D., Richardson, R. M., & Sandiford, M. (1994). On the gravitational
311 potential of the Earth's lithosphere. *Tectonics*, 13, 929–945.
- 312 Cochran, E. S., Wickham-Piotrowski, A., Kemna, K. B., Harrington, R. M.,
313 Dougherty, S. L., & Castro, A. F. P. (2020). Minimal clustering of injection-
314 induced earthquakes observed with a large-n seismic array. *Bull. Seism. Soc.*
315 *Am.*, 110, 2005–2017.
- 316 Crowell, B. W., Bock, Y., Sandwell, D. T., & Fialko, Y. (2013). Geodetic investiga-
317 tion into the deformation of the Salton Trough. *J. Geophys. Res.*, 118, 5030–
318 5039.
- 319 Di Toro, G., Han, R., Hirose, T., De Paola, N., Nielsen, S., Mizoguchi, K., . . . Shi-
320 mamoto, T. (2011). Fault lubrication during earthquakes. *Nature*, 471,
321 494–498.
- 322 Fialko, Y. (2015). Fracture and Frictional Mechanics - Theory. In G. Schubert (Ed.),
323 *Treatise on geophysics*, 2nd. ed., vol. 4 (pp. 73–91). Elsevier Ltd., Oxford.
- 324 Fialko, Y. (2021). Estimation of absolute stress in the hypocentral region of the 2019
325 Ridgecrest, California, earthquakes. *J. Geophys. Res.*, 126, e2021JB022000.
- 326 Fialko, Y., & Jin, Z. (2021). Simple shear origin of the cross-faults ruptured in the
327 2019 Ridgecrest earthquake sequence. *Nature Geoscience*, 14, 513–518.
- 328 Fialko, Y., Rivera, L., & Kanamori, H. (2005). Estimate of differential stress in the
329 upper crust from variations in topography and strike along the San Andreas
330 fault. *Geophys. J. Int.*, 160, 527–532.
- 331 Freund, R. (1970). Rotation of strike slip faults in Sistan, southeast Iran. *The Jour-*

- 332 *nal of Geology*, 78, 188–200.
- 333 Gonzalez-Ortega, A., Fialko, Y., Sandwell, D., Alejandro Nava-Pichardo, F.,
 334 Fletcher, J., Gonzalez-Garcia, J., ... Funning, G. (2014). El Mayor-Cucapah
 335 (M_w 7.2) earthquake: Early near-field postseismic deformation from InSAR and
 336 GPS observations. *J. Geophys. Res.*, 119, 1482–1497.
- 337 Hatch-Ibarra, R. L., Abercrombie, R. E., Ruhl, C. J., Smith, K. D., Hammond,
 338 W. C., & Pierce, I. K. (2022). The 2016 Nine Mile Ranch Earthquakes: Haz-
 339 ard and Tectonic Implications of Orthogonal Conjugate Faulting in the Walker
 340 Lane. *Bull. Seism. Soc. Am.*, 112, 1727–1741.
- 341 Hauksson, E., Stock, J. M., & Husker, A. L. (2022). Seismicity in a weak crust: the
 342 transtensional tectonics of the Brawley Seismic Zone section of the Pacific–
 343 North America Plate Boundary in Southern California, USA. *Geophys. J. Int.*,
 344 231, 717–735.
- 345 Herzig, C. T., & Jacobs, D. C. (1994). Cenozoic volcanism and two-stage extension
 346 in the Salton trough, southern California and northern Baja California. *Geol-*
 347 *ogy*, 22, 991–994.
- 348 Jennings, C., & Bryant, W. (2010). *Fault Activity Map of California*. (California Di-
 349 vision of Mines and Geology, Geologic Data Map No. 6)
- 350 Jin, Z., & Fialko, Y. (2020). Finite slip models of the 2019 Ridgecrest earthquake
 351 sequence constrained by space geodetic data and aftershock locations. *Bull.*
 352 *Seism. Soc. Am.*, 110, 1660–1679.
- 353 Jin, Z., Fialko, Y., Yang, H., & Li, Y. (2023). Transient deformation excited by the
 354 2021 M7.4 Maduo (China) earthquake: Evidence of a deep shear zone. *J. Geo-*
 355 *phys. Res.*, 128, e2023JB026643.
- 356 Lapusta, N., & Rice, J. (2003). Nucleation and early seismic propagation of small
 357 and large events in a crustal earthquake model. *J. Geophys. Res.*, 108.
- 358 Leloup, P. H., Lacassin, R., Tapponnier, P., Schärer, U., Zhong, D., Liu, X., ...
 359 Trinh, P. T. (1995). The Ailao Shan-Red River shear zone (Yunnan, China),
 360 Tertiary transform boundary of Indochina. *Tectonophysics*, 251(1), 3–84.
- 361 Liang, C., Ampuero, J.-P., & Pino Muñoz, D. (2021). Deep ductile shear zone facil-
 362 itates near-orthogonal strike-slip faulting in a thin brittle lithosphere. *Geophys.*
 363 *Res. Lett.*, 48, e2020GL090744.
- 364 Lindsey, E. O., Sahakian, V. J., Fialko, Y., Bock, Y., Barbot, S., & Rockwell, T. K.

- (2014). Interseismic strain localization in the San Jacinto fault zone. *Pure and Applied Geophysics*, 171(11), 2937–2954.
- Martel, S. J. (1999). Mechanical controls on fault geometry. *J. Struct. Geol.*, 21, 585–596.
- McGill, S. F., Allen, C. R., Hudnut, K. W., Johnson, D. C., Miller, W. F., & Sieh, K. E. (1989). Slip on the Superstition Hills fault and on nearby faults associated with the 24 November 1987 Elmore Ranch and Superstition Hills earthquakes, southern California. *Bull. Seism. Soc. Am.*, 79, 362–375.
- Middleton, T. A., & Copley, A. (2014). Constraining fault friction by re-examining earthquake nodal plane dips. *Geophys. J. Int.*, 196, 671–680.
- Morton, D., & Matti, J. (1993). Extension and contraction within an evolving divergent strike slip fault complex: The San Andreas and San Jacinto fault zones at their convergence in Southern California. In R. J. W. R. E. Powell & J. C. Matti (Eds.), *The san andreas fault system: Displacement, palinspastic reconstruction, and geologic evolution* (pp. 217–230). Geological Society of America Memoir.
- Mount, V., & Suppe, J. (1987). State of stress near the San Andreas fault: Implications for wrench tectonics. *Geology*, 15, 1143–1146.
- Nadeau, R. M., & McEvilly, T. V. (1999). Fault slip rates at depth from recurrence intervals of repeating microearthquakes. *Science*, 285, 718–721.
- Nur, A., Ron, H., & Scotti, O. (1986). Fault mechanics and the kinematics of block rotations. *Geology*, 14, 746–749.
- Rice, J. R. (2006). Heating and weakening of faults during earthquake slip. *J. Geophys. Res.*, 111, B05311.
- Ross, Z. E., Idini, B., Jia, Z., Stephenson, O. L., Zhong, M., Wang, X., ... others (2019). Hierarchical interlocked orthogonal faulting in the 2019 Ridgecrest earthquake sequence. *Science*, 366, 346–351.
- Schoenball, M., & Ellsworth, W. L. (2017). A systematic assessment of the spatiotemporal evolution of fault activation through induced seismicity in Oklahoma and southern Kansas. *J. Geophys. Res.*, 122, 10–189.
- Scholz, C. H. (2019). *The mechanics of earthquakes and faulting*. New York, NY: 3rd Ed., 493 pp., Cambridge Univ. Press.
- Scholz, C. H., & Choi, E. (2022). What comes first: The fault or the ductile shear

- 398 zone? *Earth Planet. Sci. Lett.*, 577, 117273.
- 399 Schubert, E., Sander, J., Ester, M., Kriegel, H. P., & Xu, X. (2017). DBSCAN re-
400 visited, revisited: why and how you should (still) use DBSCAN. *ACM Trans-
401 actions on Database Systems (TODS)*, 42, 1–21.
- 402 Segall, P. (2010). *Earthquake and volcano deformation*. Princeton University Press.
- 403 Sibson, R. H. (1974). Frictional constraints on thrust, wrench and normal faults.
404 *Nature*, 249, 542–544.
- 405 Sibson, R. H. (1990). Rupture nucleation on unfavorably oriented faults. *Bull.
406 Seism. Soc. Am.*, 80, 1580–1604.
- 407 Sibson, R. H. (1994). An assessment of field evidence for byerlee friction. *Pure Appl.
408 Geophys.*, 142, 645–662.
- 409 Skoumal, R. J., Kaven, J. O., & Walter, J. I. (2019). Characterizing seismogenic
410 fault structures in Oklahoma using a relocated template-matched catalog. *Seis-
411 mol. Res. Lett.*, 90, 1535–1543.
- 412 Takeuchi, C., & Fialko, Y. (2012). Dynamic models of interseismic deformation and
413 stress transfer from plate motion to continental transform faults. *J. Geophys.
414 Res.*, 117, B05403.
- 415 Takeuchi, C., & Fialko, Y. (2013). On the effects of thermally weakened ductile
416 shear zones on postseismic deformation. *J. Geophys. Res.*, 118, 6295–6310.
- 417 Thatcher, W., & Hill, D. P. (1991). Fault orientations in extensional and conjugate
418 strike-slip environments and their implications. *Geology*, 19, 1116–1120.
- 419 Townend, J., & Zoback, M. (2000). How faulting keeps the crust strong. *Geology*,
420 28, 399–402.
- 421 Twiss, R., & Moores, E. (1992). *Structural geology*. New York, NY: W.H. Freeman.
- 422 Tymofyeyeva, E., & Fialko, Y. (2018). Geodetic evidence for a blind fault segment
423 at the Southern end of the San Jacinto Fault Zone. *J. Geophys. Res.*, 123,
424 878–891.
- 425 Valeroso, L., Improta, L., Chiaraluce, L., Di Stefano, R., Ferranti, L., Govoni, A., &
426 Chiarabba, C. (2009). Active faults and induced seismicity in the Val d’Agri
427 area (Southern Apennines, Italy). *Geophys. J. Int.*, 178, 488–502.
- 428 Walsh, J., & Watterson, J. (1988). Dips of normal faults in British Coal Measures
429 and other sedimentary sequences. *Journal of the Geological Society*, 145, 859–
430 873.

431 Wernicke, B. (1995). Low-angle normal faults and seismicity: A review. *J. Geophys.*
432 *Res.*, *100*, 20159–20174.

433 Wessel, P., Smith, W. H. F., Scharroo, R., Luis, J., & Wobbe, F. (2013). Generic
434 Mapping Tools: Improved Version Released. *Eos, Trans. AGU*, *94*, 409–410.

435 Yang, W., & Hauksson, E. (2013). The tectonic crustal stress field and style of fault-
436 ing along the Pacific North America Plate boundary in Southern California.
437 *Geophys. J. Int.*, *194*, 100–117.

438 Yue, H., Lay, T., & Koper, K. D. (2012). En échelon and orthogonal fault ruptures
439 of the 11 april 2012 great intraplate earthquakes. *Nature*, *490*, 245–249.

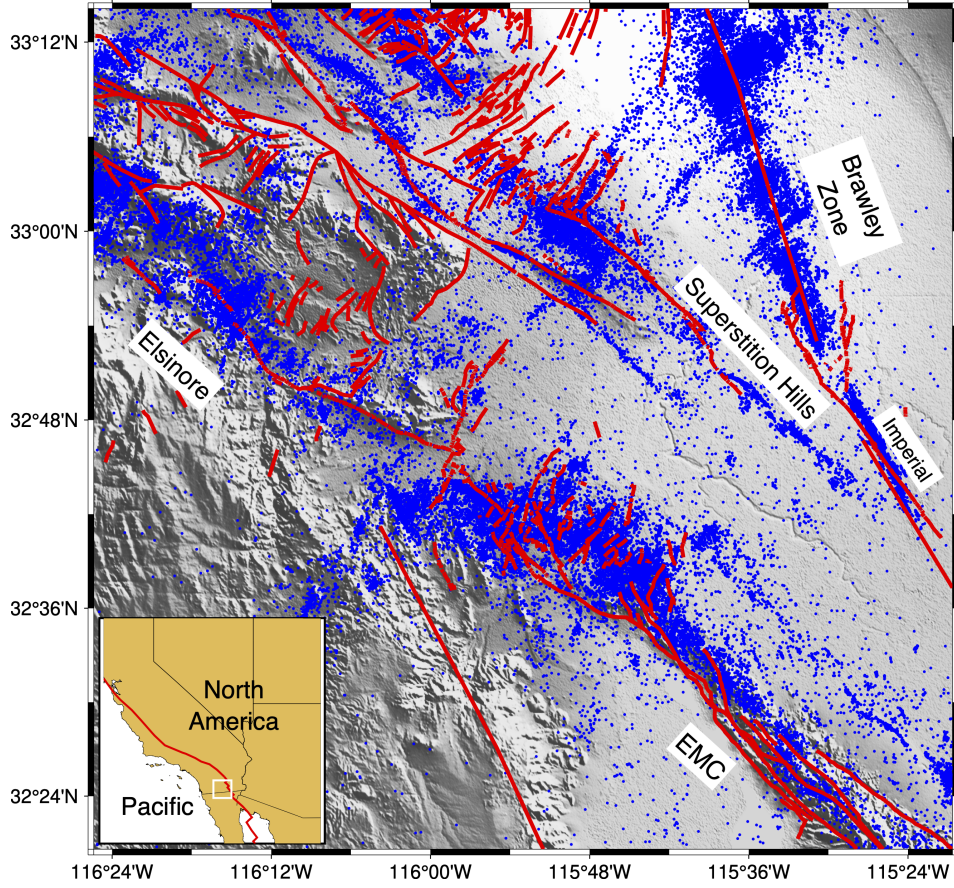


Figure 1. Map of the study area, with shaded relief. Red lines denote traces of Quaternary faults (Jennings & Bryant, 2010). Blue dots denote earthquake epicenters from Cheng et al. (2023) catalog. EMC=“El Mayor-Cucapah”. The inset shows the regional setting with respect to the North America-Pacific plate boundary (red line).

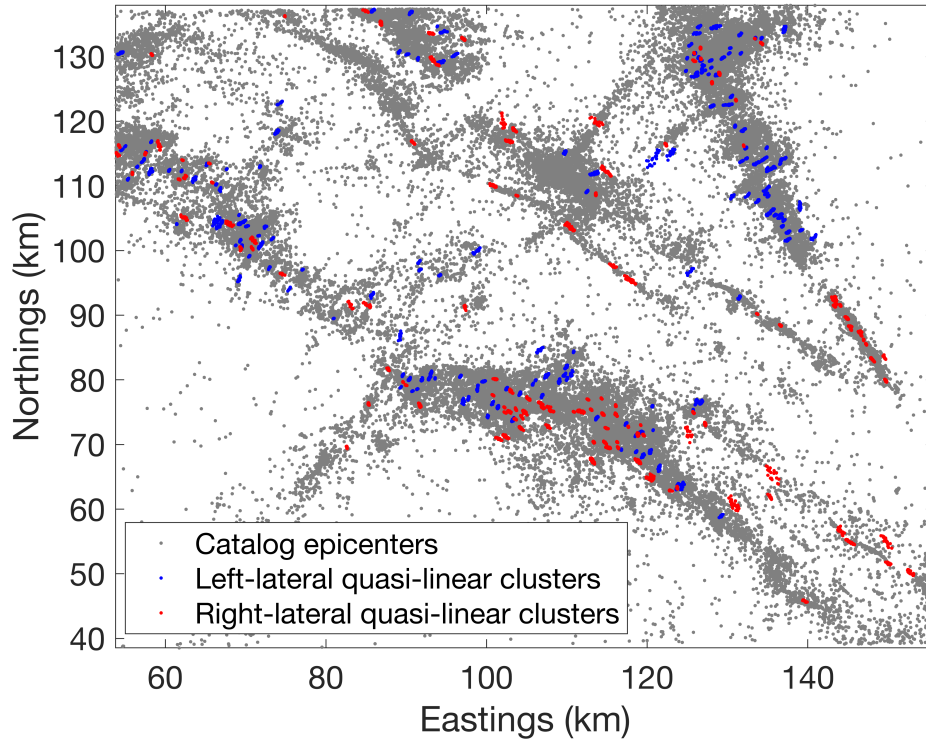


Figure 2. Grey dots: catalog epicenters (same as in Figure 1). Red and blue dots: quasi-linear clusters of epicenters with right- and left-lateral sense of slip, respectively, identified by our analysis. A total of 332 clusters are shown, including 195 left-lateral clusters and 137 right-lateral clusters. The minimum and maximum cluster lengths are 76 m and 3.05 km, respectively.

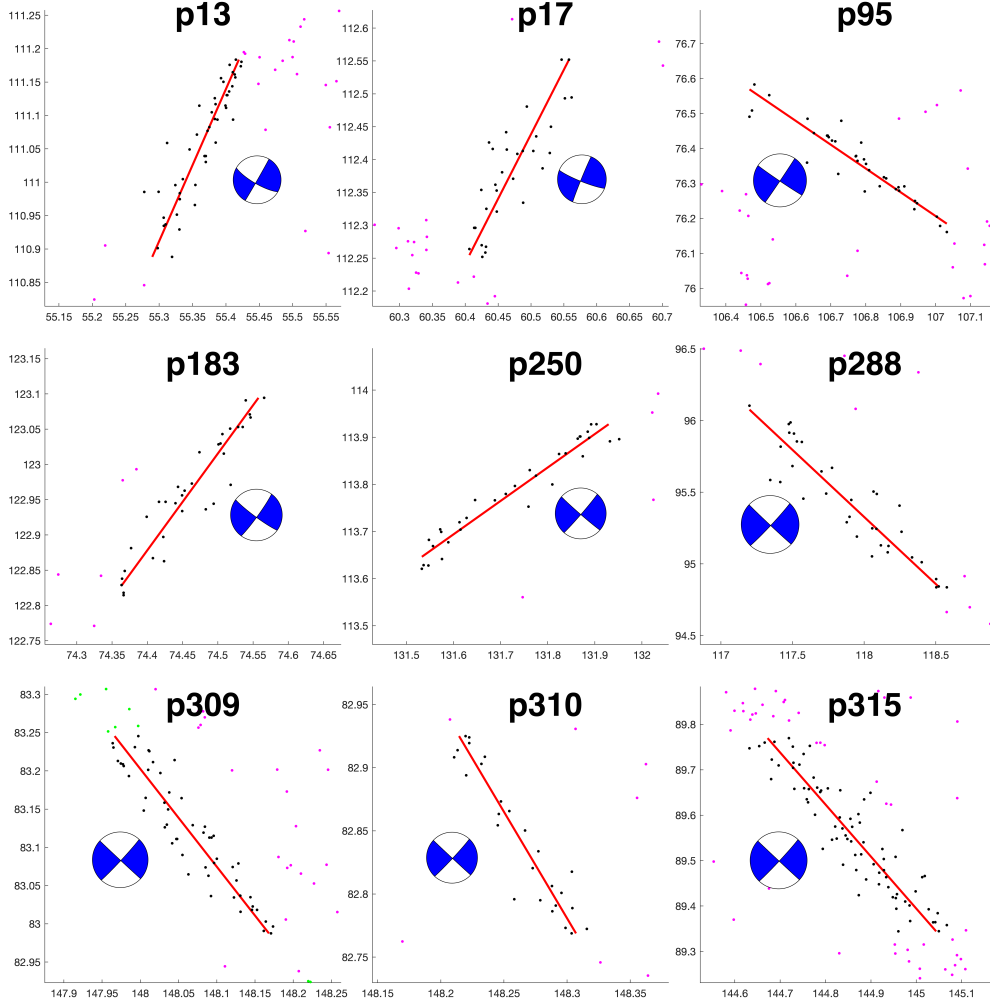


Figure 3. Examples of quasi-linear clusters (QLCs) that passed the quality control checks. Black dots denote earthquakes constituting a cluster, and magenta dots denote the background seismicity. Red lines denote best-fitting linear segments. Blue beach balls denote composite focal mechanisms. Numerical labels denote cluster numbers (see Supplementary Figures S5-S16). Axes represent northing and easting coordinates, in km.

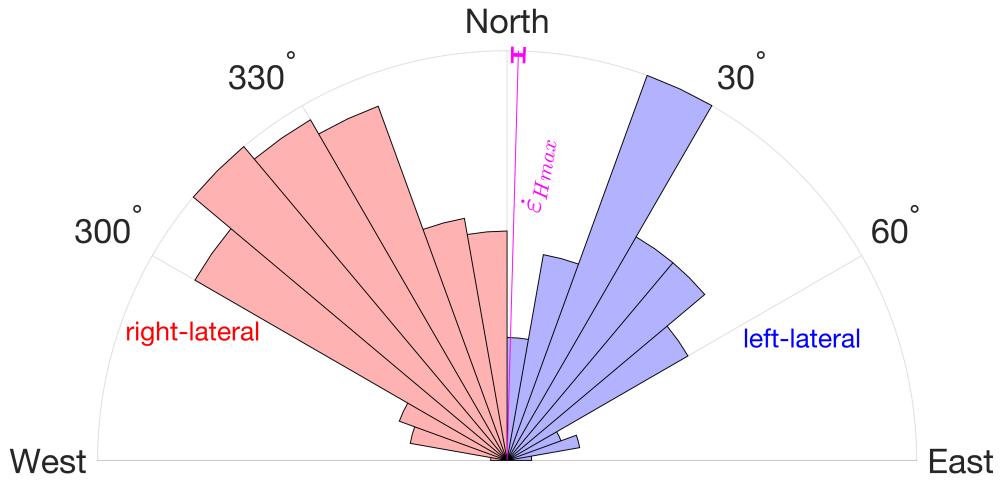


Figure 4. A distribution of strike angles of high-quality QLCs shown in Figures 3 and S4-S16. Red histogram corresponds to right-lateral faults (total of 137 samples), and blue histogram corresponds to left-lateral faults (total of 195 samples). Thin magenta line denotes the average orientation of the principal shortening rate axis (see Figure S3). The magenta error bar denotes 4 standard deviations.

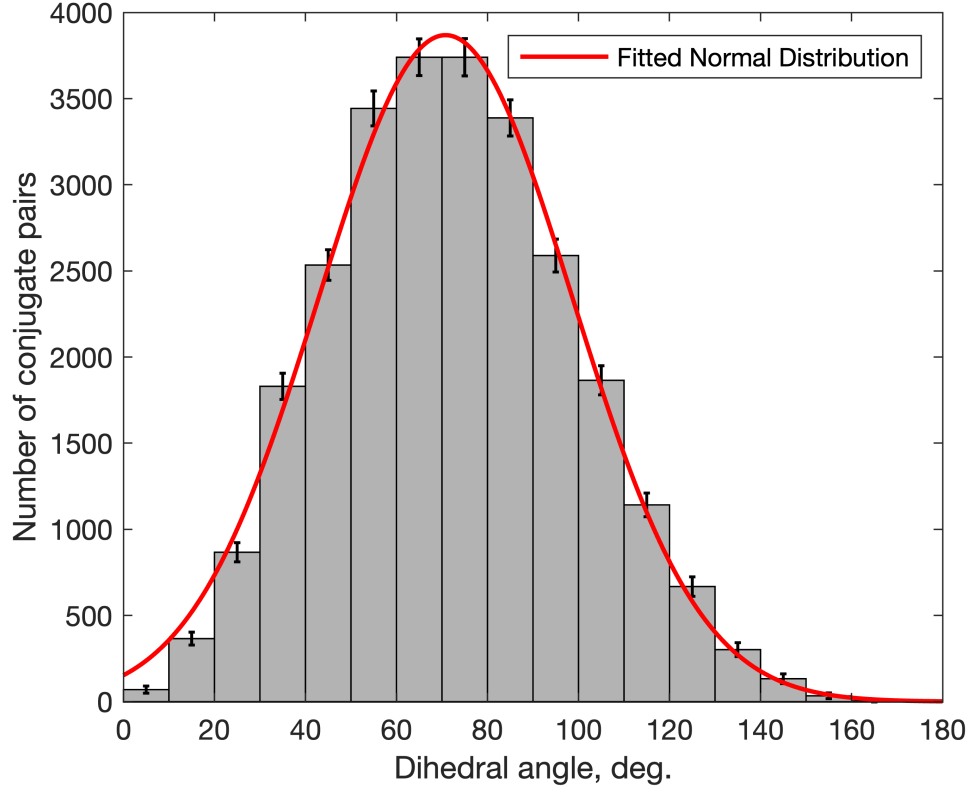


Figure 5. A histogram of dihedral angles between the conjugate strike-slip faults shown in Figure 4. Dihedral angles were computed between every possible pair of right- and left-lateral faults. Error bars denote 2σ uncertainty (see Fialko (2021) for details of the error analysis). The red curve denotes the best-fitting Gaussian distribution. The mean is 70.8 and the standard deviation is 28.9 degrees.